Journal of Geophysical Research: Earth Surface

RESEARCH ARTICLE
10.1029/2018JF004676

X-Band Radar Mapping of Morphological Changes at a Dynamic Coastal Inlet

Peter Rogowski[1], Tony de Paolo[1], Eric Terrill[1], and Jesse McNinch[2]

[1]Coastal Observing R&D Center, Marine Physical Laboratory, Scripps Institution of Oceanography, La Jolla, CA, USA, [2]USACE Field Research Facility, Duck, NC, USA

Key Points:
- Inlet shoals were mapped using time-averaged X-band radar observations with mean spatial absolute errors of at least 4.3 m
- Observed shoal migration estimates of 2–3 m/day were consistent with model results and a previous morphology study at the New River Inlet
- Across-shoal position errors were found to be a function of complex interactions between bathymetry, tidal flow, and waves

Correspondence to:
P. Rogowski,
progowski@ucsd.edu

Citation:
Rogowski, P., de Paolo, T., Terrill, E., & McNinch, J. (2018). X-band radar mapping of morphological changes at a dynamic coastal inlet. *Journal of Geophysical Research: Earth Surface*, *123*, 3034–3054. https://doi.org/10.1029/2018JF004676

Received 13 MAR 2018
Accepted 24 OCT 2018
Accepted article online 31 OCT 2018
Published online 23 NOV 2018

Abstract Remote sensing of the complex interactions between bathymetry, tidal flow, and waves in coastal inlets provides high-resolution data sets that can be exploited to characterize the morphological variability of shallow ebb tidal deltas (ETD). Here we used observations from a mobile X-band radar platform to determine optimal conditions during which radar-derived shoal signatures best represent positions of underlying shoals. Significant increases in the spatial errors of radar shoal signatures were observed when offshore wave energy intensified. Consequently, the lowest spatial errors occurred when the radar shoal signatures were primarily a function of the tidal flow (i.e., low sea state). We used these findings to quantify shoal migration patterns at the New River Inlet, North Carolina. We found that the southwestern portion of the ETD had the largest morphological variability with typical shoreward migration rates of 2–3 m/day driven by incident wave energy. The migration rates and patterns estimated from X-band observations were consistent with numerical modeling results and a previous video-based New River remote sensing study. Our results confirm that X-band radar can be used to quickly map shallow ETDs (e.g., 5 min of observations), allowing for rapid morphological assessments from shore or boat-based platforms. The methods would prove particularly useful for initial assessment as well as continual monitoring of dynamic tidal inlets where large morphological responses can be rapidly assessed and used for geomorphological studies, and as decision aids for maritime or engineering operations.

Plain Language Summary The manuscript presents a method for determination of the appropriate times when X-band-derived shoal signature positions best correlate with underlying (true) shoal positions. When these times are defined, small-scale shoal features can be tracked and their spatial and temporal migration patterns assessed.

1. Introduction

Tidal inlets serve as a transitional region connecting the open ocean to bays, lagoons, marshes, and tidal creek systems. They are of great ecological and economic importance serving as navigational routes, nutrient/pollution exchanges, and migration pathways for fish and larvae. Persistent observations of morphological variability and circulation patterns are essential for proper coastal management, recreational safety, and naval operations (Dodet et al., 2013). Inlets can migrate rapidly, on the order of days, forced by wave-driven littoral transport (Cayocca, 2001; Hayes, 1991; Lippmann & Holman, 1990) making monitoring through traditional in situ methods a challenge. As a result, numerous studies have used empirical and conceptual models that have increased the understanding of the overall mechanisms driving the circulation in these tidal inlet regions (e.g., Bruun, 1978; Bruun & Gerritsen, 1960; Dodet et al., 2013; FitzGerald, 1988; Gao & Collins, 1994; Goodwin, 1996; Hoan et al., 2011; Keulegan, 1951; Nahon et al., 2012; O'Brien, 1931, 1969; Ridderinkhof et al., 2016; Tung et al., 2009). Yet a physics-based understanding of the forces driving morphological changes remains unclear. In particular, wave-current interactions and the feedback with the ebb tidal delta (ETD) morphology due to storm events are poorly understood (Cayocca, 2001; McNinch et al., 2012). The inability to account for high-frequency (days) bathymetric variability within numerical models is known to cause large forecast errors, which is a fundamental impediment to operational applications of forecast models (Allard et al., 2008; Austin et al., 2012; Wilson et al., 2010, 2014). Regular monitoring of inlets can close this scientific gap by providing data sets for numerical model assessments.

Wave-dominated inlets are forced by the combination of waves, tides, and shallow waters (i.e., bathymetry) leading to rapid morphological changes over short time periods (Bertin et al., 2009). For example, strong morphological responses are evident for several Portuguese tidal inlets, where the interactions of a severe wave

climate, with a mesotidal range and shallow channels, result in channel migration reaching 200 m within a few months (Oliveira et al., 2006). Similarly, the Katama inlet in Massachusetts was observed to migrate at an average rate of 375 m/year from 2007 to 2014 (Nienhuis & Ashton, 2016). Like wave-dominated inlets, seasonally open inlets experience significant migration rates over short periods of time (Cooper, 1994; FitzGerald, 1988; Ranasinghe et al., 1999, Ranasinghe & Pattiaratchi, 2003). Routine monitoring of these coastal inlets using traditional in situ methods is generally not feasible due to cost restrictions, synoptic observational requirements, hazards, and logistical limitations. These challenges provide strong motivation for cost-effective remote sensing techniques that can continuously monitor nearshore regions under most environmental conditions, providing a valuable tool for long-term monitoring (see review in Holman & Haller, 2013). Common remote sensing monitoring methods include optical imagery collected from shore-based towers (Holman & Stanley, 2007), infrared (Chickadel et al., 2009), light detection and ranging (Blenkinsopp et al., 2012), airborne platforms (Dugan et al., 2001), and radar (Catalán et al., 2011; Haller et al., 2013; Puleo et al., 2003). The broad spatial coverage, synoptic observations, and temporal range of these platforms provide insights not available from traditional in situ instruments.

While large-scale morphological behavior of inlets has been routinely studied using numerical models (Cayocca, 2001; Elias & Spek, 2006; Ranasinghe & Pattiaratchi, 2003; Siegle et al., 2007; Van Leeuwen et al., 2003; Van der Vegt et al., 2006; Wang et al., 1995), smaller scale morphology studies (10–100 m) in tidal environments are infrequent in the literature. Ruessink et al. (2002) performed a small-scale study using time-exposure X-band images to estimate locations of underlying sandbar crests off the coast of Egmond aan Zee, Netherlands, however, the study area was nontidal. An exception is an optical-based morphological analysis of the New River inlet utilizing a remote sensing Argus system that overlooked the southwestern (SW) portion of the inlet. In the 23 days of data collection during the RIVET experiment the authors' observed shallow features to migrate in a clockwise direction at migration rates typically above 1 m/day, with a maximum observed rate of 3.5 m/day (Pianca et al., 2014).

Here we report on marine X-band radar observations of the New River Inlet, North Carolina, utilized to observe morphological variability. The fieldwork was conducted during the Office of Naval Research (ONR) sponsored Inlets and Rivers Mouth Dynamics Departmental Research Initiative (RIVET-I) experiment in May 2012 (e.g., Chen et al., 2015; Feddersen et al., 2016; MacMahan et al., 2014; Pianca et al., 2014; Rogowski et al., 2014; Spydell et al., 2015; Wargula et al., 2014; Zippel & Thomson, 2015). The work uses ensemble averages of continuous X-band radar scans (42 rotations per minute) to delineate shoal positions within inlet. The data were used to assess the feasibility of quantifying migration patterns and rates of the shoals over the course of the RIVET-I experiment. We find that elevated X-band radar intensity signatures from shallow shoals inside of the ETD can serve as a proxy for shoal positions when averaged over an ebb tidal cycle or observed at the appropriate tidal stage(s) dependent on incident wave energy. High-frequency shoal movement on the order of days was observed, and its driving mechanisms are discussed.

1.1. New River Inlet, North Carolina

The New River Inlet is located within the northern region of the South Atlantic Bight, also known as the Carolina Cape region. The estuary is a broad, shallow water body with an estuarine surface area of 88 km^2, located in Onslow County, North Carolina. The estuarine waters enter the Atlantic Ocean, via the New River Inlet between two barrier islands, discharging out of a primary channel, and a previously dredged remnant channel (Figure 1). The dominant terms in the subtidal along-channel momentum balance are between the along-inlet pressure gradient and the bottom stress. The wave radiation-stresses are only significant during storms where wave breaking (increased radiation-stresses) enhances flood flows into the inlet (Wargula et al., 2014).

The semidiurnal M_2 tide is the principal tidal signal in the midshelf to inner-shelf regions of the South Atlantic Bight, contributing 80% of the kinetic energy (Pietrafesa et al., 1985). Tidal ellipses in the region are predominantly in the across-shelf direction with the tidal current decreasing shoreward where, except around the shoal regions, residuals are generally weak (Werner et al., 1999). Meteorological forcing accounts for a majority of the remaining energy (Beardsley et al., 1976). Wind stress in the Carolina Capes is strongly coupled to midshelf and inner-shelf dynamics, with both alongshore and cross-shelf currents responding to synoptic atmospheric forcing (Pietrafesa et al., 1985). The estuary is likely tidally choked with an observed 87% reduction in the amplitude of the semidiurnal tidal constituent from the ETD to the end of the channel that opens up in the back bay (MacMahan et al., 2014).

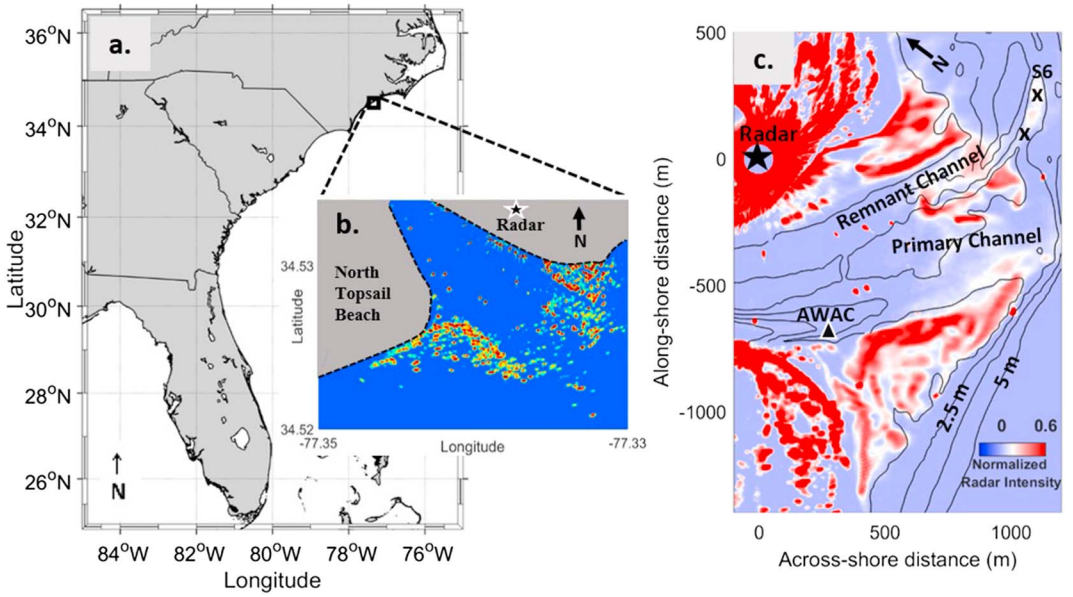

Figure 1. (a) New River Inlet site map with location within North Carolina denoted by the black box. (b) Raw X-band output on 17 May 2012. (c) Fifteen-minute ensemble-averaged radar intensity delineating areas of persistent high radar intensities rotated on a Cartesian coordinate system. S6 denotes a deeper shoal assessed at positions X in this study, while ▲ marks the location of a Woods Hole Oceanographic Institution deployed Nortek Acoustic Wave and Current Profiler (AWAC) buoy.

Additional studies from the RIVET-I experiment defined the mechanisms responsible for migration patterns within the New River ETD. Observational data showed the primary channel to be ebb dominant with strong outflow (Wargula et al., 2014). The centered seaward flow at the main channel resulted in dominant flood flows on the adjacent shallow ETD lobes, which served to transport sand into the inlet. However, the strength of the ebb flows limited transport into the inlet resulting in recirculation of sand onto the sidelobes of the ETD (Pianca et al., 2014).

The numerical modeling work of Chen et al. (2015) at the New River Inlet found sediment fluxes to be offshore directed in the channels while more complicated residual circulation patterns persisted over the ETD caused by the interactions between tidal currents, waves, and bathymetry. However, while the system was tidally dominant in the channels, waves were the primary mechanism in the generation of residual circulation patterns near the inlet entrance, enhancing offshore-directed flow in the channels and driving landward directed currents over the ETD. The resulting wave-induced circulations and alongshore currents were dominant in the nearshore region and on the ETD resulting in a clockwise circulation pattern, with landward directed flow driven by wave energy over the center of the ETD. Simulations suggested that the strength of the circulation patterns were a function of wave energy with wave-induced circulation patterns becoming insignificant (less than 0.1 m/s) when the offshore significant wave height was less than about 1 m. These circulation patterns resulted in a net offshore sediment transport in the channel, whereas the clockwise residual circulation patterns, primarily caused by interactions between waves and bathymetry, carried sediment landward or alongshore on the ETD. The New River Inlet modeling results were similar to those in Teign Inlet, United Kingdom, where the sediment transport in the channels is dependent on the spring-neap cycle, but the transport on the ETD is primarily driven by waves (Chen et al., 2015; Siegle et al., 2004).

2. Observational Data

2.1. Bathymetry and Hydrodynamics Data

Bathymetric surveys were conducted by the U.S. Army Corps of Engineers (USACE) Field Research Facility with their Lighter Amphibious Resupply Cargo vessel (LARC5). The hydrographic survey system consists of a RTK-GPS, a Knudsen 320BP fathometer equipped with a 200-kHz frequency transducer, and a TSS DMS Series 3–25 motion sensor. The amphibious LARC5, with its integrated RTK-GPS and fathometer, enabled seamless

measurements of topography and bathymetry across the shoals and channels of the New River Inlet ETD. Three bathymetry surveys were performed on 2 May 2012, 10 May 2012, and 17 May 2012 (Figures 2a–2c). The vertical control datum for bathymetry observations used at RIVET-I was the North American Vertical Datum of 1988 (NAVD88). The inlet bathymetry observations illustrate an ETD that spans approximately 2,000 m alongshore and up to 700 m offshore with depth increasing rapidly offshore (Feddersen et al., 2016). The primary navigation channel is up to 10-m deep within the inlet and shallows to 2-m depth near its exit to the ocean. The SW ETD is triangular with several shallow shoals of length around 100 m. A small flood channel runs between these shoals and the shoreline (Figure 2).

Tidal velocities were measured using a bottom-mounted Nortek Acoustic Wave and Current Profiler (AWAC) in 3.5-m water depth deployed by the Woods Hole Oceanographic Institution (WHOI) within the primary channel (Figure 1c). One spring and neap cycle were observed during the experiment with maximum ebb velocities near 1.3 m/s (Figure 3a). Wave conditions were measured from a waverider buoy (CDIP Station # 190) located offshore in 13-m depth (34.48°N, 77.30°W). During the experiment, the mean significant wave height ranged from 0.4 to 1.5 m with a few moderate wave events of 1 m (Figure 3b). Wave periods primarily ranged from 5 to 12 s, and wave directions varied primarily from south to east (Figures 3c and 3d).

2.2. X-Band Radar

A mobile radar van, deployed on the northern beach adjacent to the New River Inlet, was used as an observational platform during the RIVET campaign. Instrumentation on the platform included a meteorological station (Vaisala WXT520) and an extendible radar tower consisting of a Furuno X-band marine radar. Radar intensity was digitized and recorded at a 3-m range resolution and 1/12° angular resolution by a Wave and Surface Current Monitoring System (WAMOS) digitizer with 1,024 range samples taken at each beam angle for an approximate total range of 3 km from the source. The postdigitization video gain for WAMOS is typically used in low wind conditions to create a larger bit depth/dynamic range in the recorded images. It is set prerecording and cannot be postprocessed, and typically is set so the ocean backscatter signal is in the middle of the digitized data range. We adopted a local coordinate system that was aligned with the shoreline south of the inlet with $+x$ in the offshore direction (rotated 148° relative to true north) and $+y$ in an alongshore direction (northeastward). It was the same local coordinate system used by several other RIVET studies (e.g., Feddersen et al., 2016; Pianca et al., 2014; Zippel & Thomson, 2015): however, the X-band radar location is used as our origin. This study included 19 consecutive days (2 May to 20 May 2012) of X-band radar data. Each polar scan was ~10 MB, which returned ~21 GB of data per hour for a total ~10 TB collected over the campaign.

2.2.1. X-Band Shoal Signatures

Radar backscatter from the ocean surface is mainly caused by small-scale roughness of the sea surface, which is mostly generated by the local surface wind (Dankert et al., 2005). The resulting capillary waves on the sea surface that cause Bragg-scattering of the incoming radar energy are modulated by surface gravity waves (Bass et al., 1968; Wright, 1968). However, many observations show scattering signatures that are not consistent with Bragg scattering or composite surface theory. These anomalies include high-intensity bursts of intensity (sea spikes) often attributed to wave breaking (Catalán et al., 2011), which can be averaged to map areas of persistent breaking.

Time exposure imaging has been used for visualizing and measuring nearshore morphology on open beaches since its introduction in 1989 (Lippmann & Holman, 1989). By averaging a sequence of images over a time period substantially longer than the period of the incident sea swell, clutter is removed, leaving patterns of enhanced wave dissipation that have been shown to correspond well to submerged sandbar or shoreline features (Holland, 1998; Holland et al., 1997; Holman et al., 1993; Lippmann et al., 1993; Lippmann & Holman, 1989; Pearre & Puleo, 2009; Pianca et al., 2014; Plant et al., 2007; Van Enckevort & Ruessink, 2003a, 2003b). Likewise, instantaneous X-band radar observations can be averaged over similar periods (e.g., several minutes) to produce maps of persistent high-intensity regions that delineate inlet features (Bell et al., 2016; McNinch et al., 2012; Ruessink et al., 2002). Similar to the optical video technique (Lippmann & Holman, 1989; Van Enckevort & Ruessink, 2003a), shoal locations can be estimated from the peak value of across-shoal intensity. In addition, time averages of surface perturbations resulting from the interaction of the overlying flow with bottom topography can be used to assess shoal

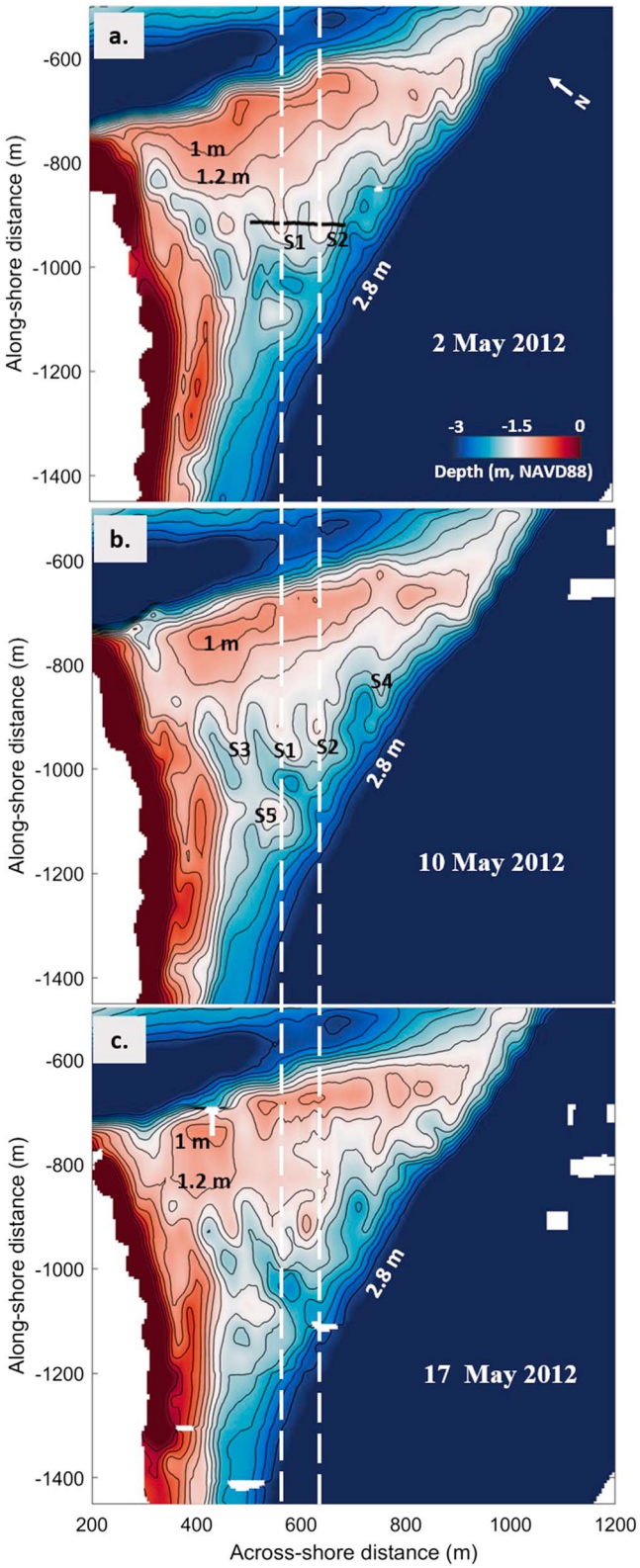

Figure 2. Bathymetry of southwestern portion of the ebb tidal delta (from the U.S. Army Corps of Engineers Field Research Facility) as measured on (a) 2 May 2012 and (b) 10 May 2012, and (c) 17 May 2012. The black horizontal line in (a) denote the location of a transect used to assess the tidal error patterns in radar-derived shoal positions of the underlying shoals S1 and S2. The vertical lines denote lines of constant alongshore distance used for visual comparisons of the two shoals on 2 May, 10 May, and 17 May 2012. Labels in (b) denote shoals with observed migration during the experiment. The contour lines are given in 0.2-m intervals.

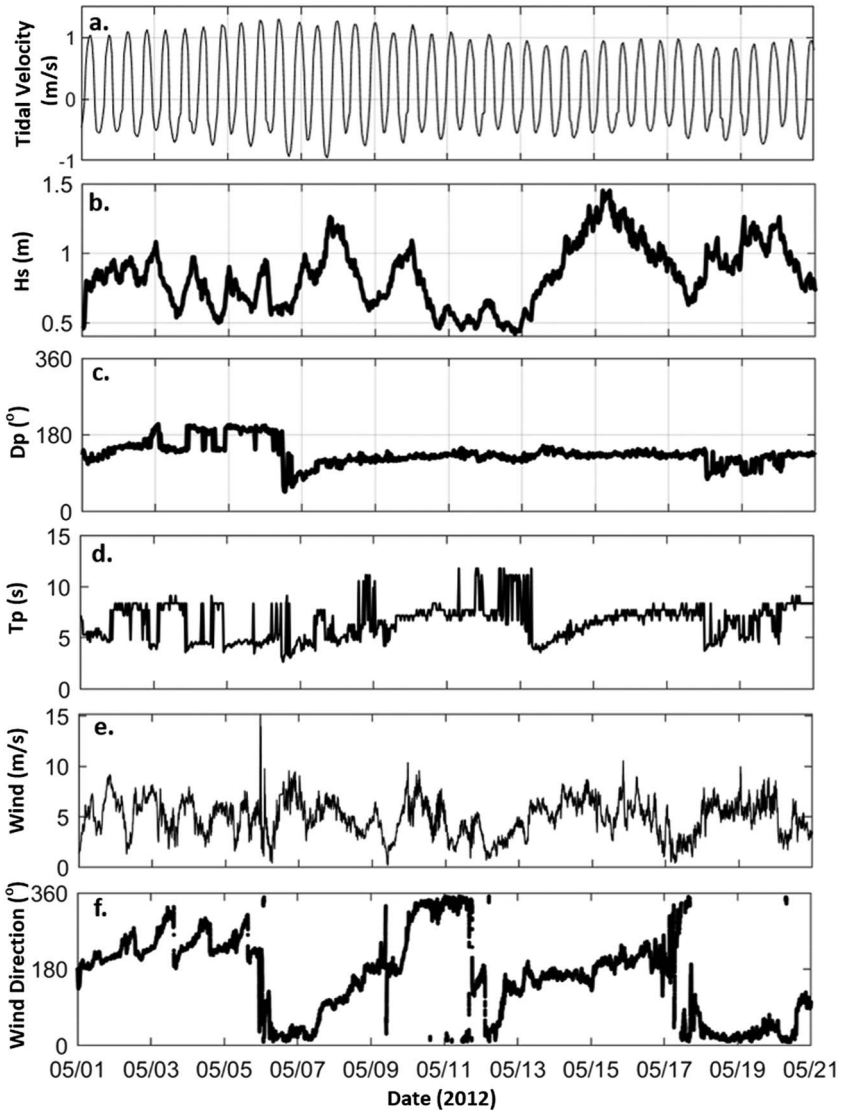

Figure 3. Environmental condition summary during the RIVET experiment including time series of (a) tidal velocity, (b) significant wave height, (c) peak wave direction, (d) peak wave period, (e) wind speed, and (f) wind direction. A CDIP buoy offshore of New River Inlet measured wave statistics and wind observations were made locally at the radar location.

morphodynamics in the absence of wave breaking (e.g., flood/ebb tides). These perturbations induce variations in the surface wavefield that appear as intensity modulations in the radar imagery (Alpers & Hennings, 1984; Donato et al., 1997). Nonstationarity problems are avoided as the averaging period of several minutes is considerably less than the time scale of significant shoal migration.

Given its prevalence in the morphological literature, time exposure imaging of X-band radar observations was the method selected for our analysis. Raw radar scans are averaged over 15-min intervals (~630 scans) to delineate areas of persistently high radar intensities within the New River Inlet (i.e., surface shoal signatures). The signatures are dependent on incident wave energy, tidal depth, and shoal position. If the position of the shoal and wave height remains constant, a tidal error would show erroneous movement due to shifting regions of persistent breaking (McNinch, 2007). We leverage the shoal signature response from time-averaged X-band radar images to determine the optimal times in which radar-derived shoal signature positions best represent true shoal positions. We selected the 15-min averaging interval to reduce clutter; however, the averaging interval was spatially consistent with higher resolution averages (e.g., 5 min).

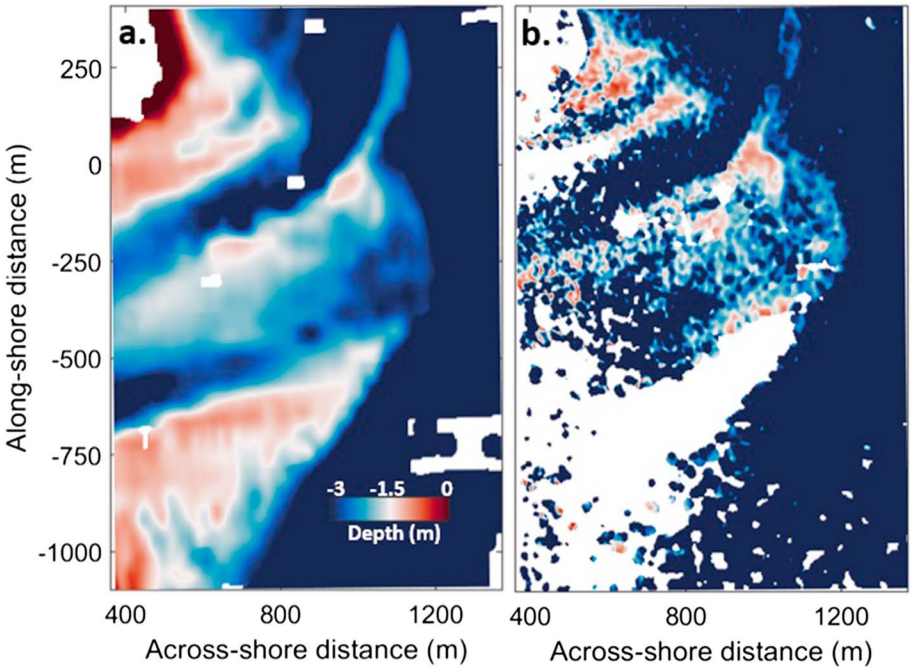

Figure 4. (a) Bathymetry data on 17 May 2012 and (b) estimated bathymetry on 17 May 2012 using the cBathy algorithm with X-band observations as input. Areas of missing data denote regions where the cBathy algorithm failed to converge on a solution.

3. Methods

X-band radar bathymetry inversion techniques have routinely been used to estimate morphology along open coastlines (e.g., Bell, 1999; Bell et al., 2006). However, application of these techniques in ETD regions remains a challenge due to complex bathymetry, wave, and current interactions generated from tidal flows. At the New River Inlet, we tested the cBathy algorithm described by Holman et al. (2013) to assess the ability of the algorithm to estimate bathymetry of the shallow shoaling regions using X-band radar intensity observations over the inlet. The algorithm consistently failed to converge on solutions within the shallow SW portion of the ETD (Figure 4). The numerical modeling results from Chen et al. (2015) found rapid onshore decay of wave heights over this region resulting from wave breaking along the breaker zone of the ETD whose location is modulated by the tidally varying water depths (~2-m contour). The cBathy algorithm uses the dispersion relationship to estimate depth and is solved numerically if both wavelength (L) and wave period (T) are known. However, in very shallow water ($<$L/20), waves become nondispersive (celerity independent of frequency), and the nonlinear behavior of breaking waves and wave-current and bathymetry interactions violate underlying assumptions of the dispersion relation (Bergsma et al., 2016).

While the cBathy algorithm was originally developed for open ocean beaches that neglects the effects of currents, Holman and Stanley (2013) used an extension of the dispersion relationship to account for mean currents and estimate bathymetry from video imagery at the New River Inlet. Their work served as an initial test of the cBathy algorithm in a tidal environment where both bathymetry and tidal currents affect the speed of wave propagation. Initial analyses showed up to 50% overestimation of depth excursions without Doppler corrections presumably due to wave-current effects. They utilized data from in situ instruments to assess the adjustments needed to account for the Doppler correction, which they found explained some of the bias. In general, the overall pattern of the ETD was well described by the cBathy algorithm, but errors in absolute depths of small-scale features (i.e., within the SW ETD) were prevalent (Holman & Stanley, 2013). We define small-scale features within these shallow regions as 100 m or less.

Bergsma et al. (2016) found significant differences in cBathy bathymetry estimates between spring and neap tidal cycles in a macrotidal environment. They present methods to modify the cBathy algorithm resulting in substantial improvements in accuracy. However, they also found less accurate results in the shallow regions

where the dispersion relation breaks down. At the New River Inlet, mean wave periods were typically larger than 5 s (Figure 3d), resulting in a minimum threshold depth in the dispersion relation of approximately 2 m, suggesting that inversion techniques are not applicable to the shallow SW portion of the ETD (Figure 4).

Due to the challenges of accurately estimating small-scale features in a complex tidal delta with inversion techniques, we assessed the feasibility of utilizing X-band radar-derived shoal signatures to accurately track the small-scale migrating features within the New River ETD. Specifically, (1) determination of optimal times in which radar derived shoal positions best represented true shoal positions and (2) quantification of shoal migration within the New River Inlet. Three bathymetry surveys served as ground-truth data sets for comparisons to radar shoal signatures.

Visual inspection of the bathymetry surveys revealed a net shoreward movement ($-x$ direction) of several shoals within the ETD from 2 May 2012 to 17 May 2012 (Figure 2). As an initial assessment, one observational transect parallel to the dominant direction of movement of shoals S1 and S2 (Figure 2a) was used to quantify temporal and spatial variability of the radar shoal signatures to ground truth shoal positions as a function of tidal current. These 1-D comparisons were extended to a more robust 2-D analysis by tracking the variability of the peak intensity in radar signatures over the shallow shoals within the SW ETD over several tidal cycles.

These analyzes provided times when radar shoal signatures best represented true shoal positions allowing for digital-particle image velocimetry (DPIV) between subsequent radar images, a common method for quantitative and qualitative displacement visualization (Buchhave, 1992; Keane & Adrian, 1990; Melville et al., 2002). We followed the method described by Duffy and Hughes-Clarke (2005), who used a modified DPIV method to track migration of submarine sand dunes. The spatial cross-correlation method can be used to locate the point where two spatial data sets are most similar. The strength of the correlation between two data sets is quantified by the discrete cross-correlation coefficient, which is computed as the sum of the products of overlapping pixels,

$$C(m,n) = \sum_i \sum_j I_1(i,j) I_2(i-m, j-n) \tag{1}$$

where I_1 and I_2 are corresponding interrogation areas from images 1 and 2, respectively. The maximum peak location in $C(m,n)$ indicates the particle displacement where the two images are highest correlated (Huang et al., 1997). To avoid errors due to variability in interrogating window size and bright or dark spots, $C(m,n)$ was normalized by subtracting the mean and dividing by the standard deviation (Duffy & Hughes-Clarke, 2005).

Prior to DPIV analysis, a radar intensity threshold of 25% of the maximum value was applied, removing low-intensity regions that could cause false positives. The initial interrogation window size (I_1) was unique to each shoal and chosen to fully encompass the targeted radar shoal signature. The size of the subsequent interrogation window (I_2) for image 2 is the same as (I_1) and steps through four offset positions in the $\pm x$ and y directions. The x and y offsets were chosen to have 50% overlap of windows in both the x and y directions to ensure redundancy in measurement.

4. Results

4.1. 1-D Spatial Variability of Radar Shoal Signatures

The feasibility of using radar intensity to track temporal changes and morphological variability within the New River Inlet was assessed by comparing the position of the ensemble-averaged radar intensity shoal signatures to observed bathymetry data. Error was defined as the spatial difference (in meters) between true shoal positions derived from bathymetry data and radar-observed shoal signature positions. To assess the feasibility of using radar shoal signatures as a proxy for shoal positions, we first analyzed the spatial and temporal variability in peak radar signatures of the two shoals along an intersecting transect (Figure 2a) over an ebb tidal cycle on 17 May 2012. Averaged (15-min) currents during each comparison period were computed from the AWAC sensor located in the primary channel. The results showed the observed variability of the radar peaks over shoals S1 and S2 during an ebb tide from 12:00 UTC to 19:00 UTC with a minimum error of 4 and 0 m for the S1 and S2 shoals, respectively (Figures 5a and 5b). Several stages of the tide exhibited good correlation between peak radar signatures to shoal position, defined by the minimum depth over the shoal, with correlation coefficients greater than 0.9 (Figure 5c).

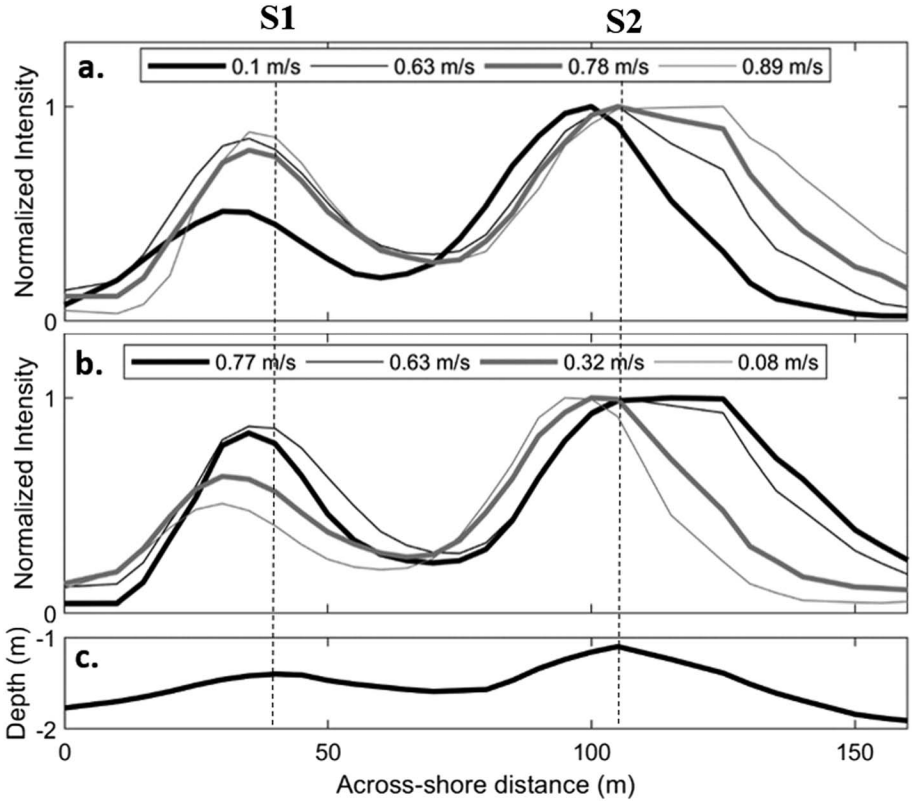

Figure 5. (a and b) 1-D ensemble-averaged (15-min) X-band normalized intensity signatures over shoals S1 and S2 underlying the transect defined in Figure 2a during ebb tide from 1200 UTC to 1900 UTC on 17 May 2012 and their corresponding averaged currents. Averaged X-band data and AWAC current data were taken at the top of every hour. (c) Collocated bathymetry data illustrating true locations of the two shoals. The vertical dotted lines denote the peak of each shoal used for ground-truth comparisons. The correlation coefficients for each radar signal starting with the 0.1 m/s signal were 0.85, 0.94, 0.9, 0.73, 0.76, 0.87, 0.89, and 0.8, respectively.

Next, we assessed the variability of radar shoal signature errors compared with current velocity and offshore wave energy (Figure 6) along our defined transect. The error calculations assumed that the positions of the shoals, as observed during the bathymetric surveys, were stationary for the comparison period. Shoal signatures resulting from shoals S1 and S2 during several tidal cycles were compared to bathymetric surveyed shoal positions from 10 May 2012 (Figures 6a and 6b) and 17 May 2012 (Figures 6d and 6e). For the former survey, we assumed no migration occurred over five tidal cycles from 9 May 2012 to 12 May 2012 due to the minimal observed sea state conditions after the 9 May 2012 (Figure 6c). Conversely, only three tidal cycles were used for comparisons from 17 May 2012 to 18 May 2012 due to more significant sea states before and after the comparison window (Figure 6f).

Shoal S1 was located within the central portion of the SW ETD sheltering it from direct interaction with the incident wavefield. However, significant wave energy (significant wave height $>$ 0.9 m) was observed to increase the position error of the shoal signature in an offshore direction (e.g., 9 May 2012; Figure 6a). Additionally, errors in an onshore direction were consistently observed during the three ebb tides from 17 May 2012 to 18 May 2012.

Assessments of the radar shoal signature errors of shoal S2, nearer the ETD ocean boundary, exhibited several different trends when compared to the more protected S1 shoal. While the same minimal error pattern during ebb was observed for the low sea state conditions after 9 May 2012, increased errors in an offshore direction again corresponded with increasing wave energy. Under these conditions, minimum errors were observed at lower ebb current velocities, nearer slack tides (Figures 6b and 6e).

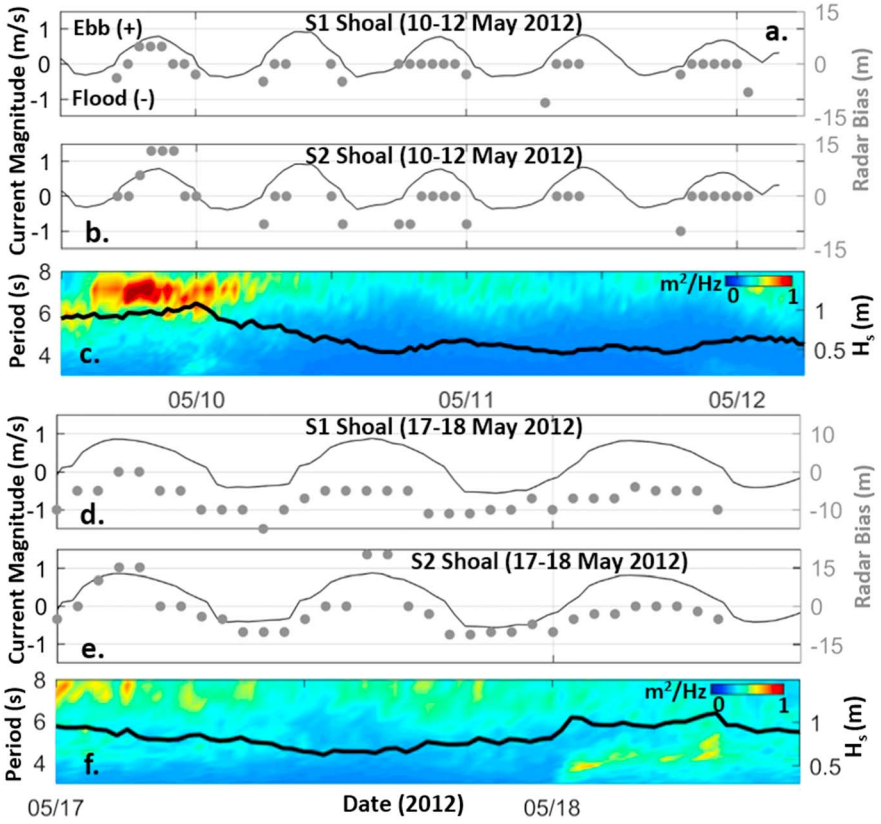

Figure 6. Time series of 1-D radar shoal signature error versus tidal current velocity along the transect illustrated in Figure 2a for (a and d) S1 and (b and e) S2 for two comparison periods when bathymetry comparison data were available, (a and b) 9 May 2012 to 12 May 2012 and (d and e) 16 May 2012 to 19 May 2012. Corresponding wave energy overlaid with H_s for each period is provided in (c) and (f).

4.2. 2-D Spatial Variability of Radar Shoal Signatures

We extended the 1-D analysis to the entire SW ETD to assess spatial variability of radar shoal signatures in the *x* and *y* directions as a function of the ebb tide for shoals labeled in Figure 2b. Similar to the 1-D analysis, we used peak radar intensity over the shoals to define a position that could be compared with bathymetry data. The spatial variability of the ensemble-averaged radar shoal signatures (15 min) for the ebb tides on 10 May 2012 and 17 May 2012 are illustrated in Figures 7a and 7b, respectively, color coded by averaged observed velocity. The 2 days experienced similar offshore wind directions; however, minimal wave energy resulted in glassy conditions that were visually observed on 10 May 2012, while observations on 17 May 2012 were made during a higher energy regime (Figures 6c and 6f). For the shallower shoals (S1, S2, and S3), radar shoal signatures consistently moved offshore (+*x* direction) with increasing tidal velocity due to the outgoing tide (Figure 7). On 10 May 2012, shoal signatures over S5 moved offshore only near maximum ebb currents; however, a different shoal signature response was observed on the 17 May 2012 due to the onshore migration of the shoal its associated bathymetric changes. The new shape of the shoal exhibits different spatial error pattern at higher current velocities resulting in a shift in position of the radar signature in the +*y* direction (Figure 7b). We also observed a larger range of variability in the *x* direction for S2 on 17 May 2012, which may be in response to the shoal being shallower by 0.3 m relative to the 10 May 2012.

4.2.1. Tidally Averaged Radar Signature Errors

The tidally averaged (ebb tide) radar shoal position errors in the *x* and *y* directions and their respective magnitudes for each shoal illustrated in Figure 7 are summarized in Table 1. Mean errors from 9 May 2012 were also included to assess the impact of a significant wave event (significant wave height $>$ 0.9 m) on radar shoal signatures. For shoals that were not defined by a unique 2-D peak, rather a ridge of shallow depths (e.g., S3 and S4), only errors in the *x* direction were computed. The table also includes mean errors for two positions

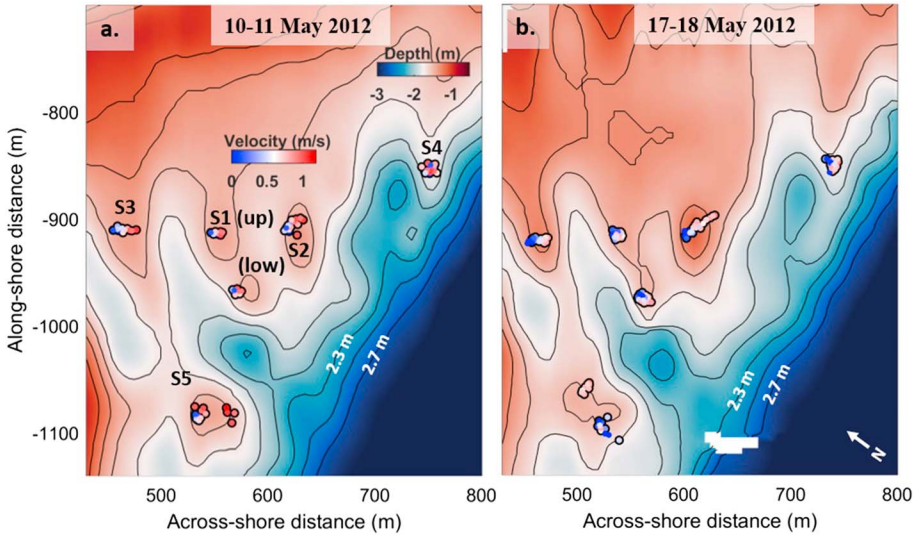

Figure 7. Bathymetry maps of the SW portion of the New River Inlet ebb tidal delta overlaid with ensemble averaged radar shoal signature locations (circles) during ebb tides on (a) 10–11 May 2012 (0600 to 1300 UTC; 1800 to 0200 UTC) and (b) 17–18 May 2012 (1200 to 1900 UTC; 0100 to 0700 UTC). Locations are color coded by averaged observed current velocity in the main channel of the inlet. Shoal labels are provided in (a).

along a deeper sixth shoal (S6), located near the exit of the remnant channel (Figure 1c). The primary direction of migration for shoals within the SW ETD was along the *x* axis, but we included *y* errors to examine the 2-D spatial consistency of the shoal signatures with respect to the actual shoal location.

The tidally averaged spatial results show that the S1 (upper) shoal had the highest degree of accuracy when compared to the true shoal position with an average *x* and *y* error over the three time periods of 2.4 and 1.2 m, respectively. Larger errors were observed for the S1 (lower) shoal with an average *x* error of 6 m over the comparison periods likely in response to changing bathymetry patterns between the two time periods.

The S2 shoal was more exposed to incident wave energy than S1 as evident in the error observed during the higher sea state conditions that existed on 9 May 2012 relative to the lower conditions on 10 May 2012 and 17 May 2012. The tidally averaged *x* errors for the two lower sea state days was 5.8 m compared with 11.9 m for 9 May 2012. In addition, the tidally averaged location of the radar shoal position was dependent on the incident wavefield. On 10 May 2012, low wave energy resulted in an average onshore *x* error of −6 m compared to a 5.4 m error in the offshore direction during higher sea states observed on 17 May 2012. Bathymetry data show that the S2 shoal is 0.3 m shallower on 17 May 2012 than what was observed on the 10 May 2012, which may also contribute to the observed variability.

Table 1
Tidally Averaged x and y Errors for Radar Shoal Signatures Within the SW ETD and Two Points Along the Deeper S6 Shoal

	9 May 12			10 May 12			17 May 12		
Shoal	*x*-error (m)	*y*-error (m)	Magnitude (m)	*x*-error (m)	*y*-error (m)	Magnitude (m)	x-error (m)	y-error (m)	Magnitude (m)
S1 (upper)	1.2	1.3	1.8	−1.4	−0.02	1.4	−4.7	2.2	5.2
S1 (lower)	−6.8	−0.97	6.9	−9.9	−2.4	10.2	−1.4	−7.7	7.8
S2	11.9	17.4	21.1	−6.1	13.7	15.0	5.4	6.4	8.4
S3	3.3	–	–	−0.48	–	–	0.74	–	–
S4	1.9	–	–	−0.38	–	–	1.9	–	–
S5	19.8	−3.6	20.1	3.4	−0.88	3.5	11.7	−2	11.9
S6 (upper)	−16.5	–	–	−3.1	–	–	−9.1	–	–
S6 (lower)	−11	–	–	−2.6	–	–	−6	–	–

Note. Errors are computed for 9 May 2012, 10 May 2012, and 17 May 2012. The magnitude of the errors is also included.

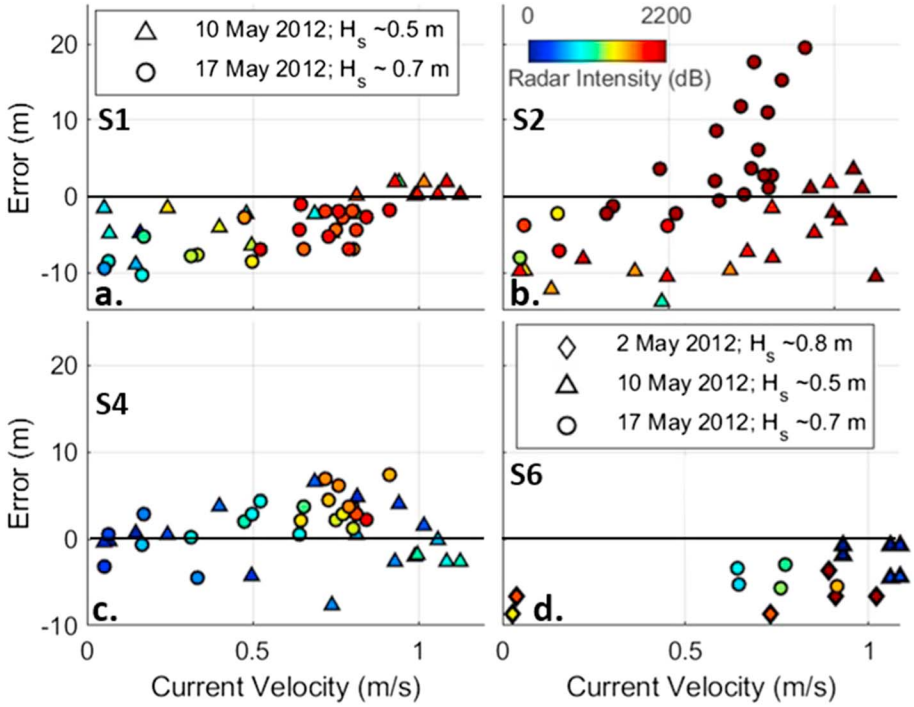

Figure 8. Scatter plots of ensemble-averaged radar errors as a function of main channel current velocity, color coded by radar intensity for shoals (a) S1 (upper), (b) S2, (c) S4, and the deeper shoal (d) S6. All plots show observations from 10 May 2012 and 17 May 2012, while (d) also includes observations from 2 May 2012.

The linear response of the shoal signatures, in the across shoal direction, to increasing ebb currents for S3 and S4 resulted in their locations being well represented by the tidally averaged ebb spatial positions regardless of sea state with mean *x* errors of 1.5 and 1.4 m.

The S5 shoal was observed to significantly change shape and size as it migrated onshore from 10 May 2012 to 17 May 2012 (Figure 7). The initial location of the shoal was accurately captured by the tidally averaged radar shoal position with an *x* and *y* error of 3.4 and −0.88 m, respectively. However, larger errors were evident on 17 May 2012 due to the change in shape and size of the shoal.

The final shoal assessed was a long (~300 m), deeper shoal (2.6 m) located near the exit of the remnant channel (Figure 1c). When tidally averaged over the ebb tidal cycles, the two positions along S6 were well characterized during the low sea state conditions on the 10 May 2012 with *x* errors of −3.1 and −2.6 m for the upper and lower positions respectively. As incident wave energy increased, so did the onshore errors with −9.1 m (upper) and −6 m (lower) observed during the moderate sea state conditions on 17 May 2012 and −16.5 and −11 m, respectively, observed during the high-energy conditions on 9 May 2012. In addition, environmental conditions on 2 May 2012 were similar to those observed on 17 May 2012 that resulted in mean *x* errors for both positions along S6 of −7 m (not shown in Table 1).

4.2.2. Ensemble-Averaged Radar Signature Errors (15-Min)

The low errors observed for S1 (upper), S3, and S4 suggest that accurate estimates of shoal position can be derived by simply tidally averaging shoal signature positions. However, the 1-D error analysis showed improvement in positional estimates for radar shoal signatures when made at specific periods within the ebb tide. Specifically, when shoals were impacted by a low incident wavefield (significant wave height < 0.6 m), radar shoal position estimates made during larger ebb currents proved to be more accurate. Conversely, when shallow shoals within the ETD interacted with higher incident wavefields, better estimates of shoal positions were made during low ebb current, near slack tide (Figure 6). To assess if better spatial accuracy of radar shoal signatures persisted for specific current velocity ranges for the 2-D analysis, radar errors were plotted as a function of current velocity and radar intensity for shoals S1, S2, S4, and S6 for observations on 10 May 2012 and 17 May 2012 (Figure 8). The improved accuracy in position of the radar shoal

Table 2
Tidally Averaged x and y Mean Absolute Error (left column) Compared to Mean Absolute Error During Optimal Comparison Time Period (right column) for S1(upper), S2, S3, and S4 Shoals

	10 May 12		17 May 12	
Shoal	*x*-error (m)	*y*-error (m)	*x*-error (m)	*y*-error (m)
S1 (upper)	2.7/1.1	0.98/1.2	5.3/3.8	2.4/2.3
S2	6.6/3.9	13.7/15	6/2.7	6.3/1.6
S3	5/4.4	–	4.4/2.4	–
S4	3.3/2.2	–	3.1/2.8	–

Note. Optimal time periods are defined by ebb currents greater than 0.9 m/s (shadowed boxes; incident wave energy not present) and between 0.25 to 0.6 m/s for the remaining boxes (incident wave energy present).

signature over S1 with increasing current was evident for both time periods, but only for 10 May 2012 observations for S2 (Figures 8a and 8b). The location of S2 nearer the ETD/ocean boundary exposed it to incident wave energy, which resulted in larger errors as the ebb current increased. The decreasing accuracy is illustrated in Figure 8b in which the shoal signature on 17 May 2012 for S2 approaches saturation at ~0.6 m/s, resulting in large position errors in the offshore direction for larger ebb currents. The scatter plots show that the optimal range when radar shoal signatures best correspond to true shoal positions is when ebb currents are greater than 0.9 m/s for S1 and between 0.25 and 0.6 m/s for S2. Shoal signatures during these optimal ranges were more consistently spatially accurate when compared to true shoal positions (Table 2).

Results from the deeper shoals, S4 (2.3 m) and S6 (2.6 m), illustrate the bias, velocity, and radar intensity relationships for each radar shoal signature (Figures 8c and 8d). While improved accuracy at S4 was seen at the highest ebb currents for the low sea state conditions on 10 May 2012, larger errors were observed for the higher currents on the 17 May 2012. The consistency of the tidally averaged spatial accuracy for S4 (Table 1) could not be improved by bounding comparison times to specific current ranges. The S6 shoal displayed a different error pattern compared to all other shoals analyzed due to its location, shape, and deeper depths. For all conditions, a negative error (onshore) was observed with the best accuracy occurring during the minimal sea state conditions on 10 May 2012, which also corresponded to the minimal radar intensity observed during our comparison periods (Figure 8d). However, a consistent error of around 7 m was observed for the similar sea state conditions on the 2 May 2012 and 17 May 2012 allowing for relative migration estimates of S6.

4.2.3. WAMOS Video Gain Settings

Flood tide radar shoal signatures were generally not found to be a good representation of the underlying shoal position. The combination of deeper depths and lower current velocities during flood tides require larger waves to produce surface signatures detectable by the radar. The flood signatures were observed during more energetic conditions from 17 May 2012 to 18 May 2012 but showed significant spatial errors in the onshore (negative) direction (Figures 6d and 6e). Conversely, low sea state conditions between 10 May 2012 and 12 May 2012 resulted in limited flood shoal signatures (Figures 6a and 6b).

The exception to these findings was the 2 May 2012 observed flood tide shoal signatures. Initial WAMOS video gain settings from 2 May 2012 to 4 May 2012 resulted in radar intensity levels over the shoals that saturated quickly at minimal ebb current velocities resulting in increasing errors with the progression of the ebb tide. However, flood tide radar shoal signatures had averaged *x* direction tidal errors of −2.3, −4.8, 3, and 1.3 m for shoals S1 (upper), S2, S3, and S4 respectively. The relatively low errors allowed us to use these position estimates in our shoal migration estimates. In addition, the consistency of the 2 May 2012 errors to the 17 May 2012 errors for the S6 suggests that the increased gain settings on 2 May 2012 did not significantly impact the spatial variability of the radar shoal signature over the deeper S6 shoal.

4.3. Shoal Migration Estimates

The spatial error analysis of radar-derived shoal signatures shows several general trends that can be leveraged to estimate shoal positions in the absence of bathymetry data. (1) The position of radar shoal signatures near maximum ebb tide when exposed to low incident wave energy best corresponds to true positions. Minimal wave exposure can result from low sea state days (e.g., 10 May 2012) or from wave energy dissipating prior to interacting with a protected inshore shoal (e.g., shoal S1). (2) When shoals interact with incident wave energy, radar shoal signature positions nearer slack tide best correspond to true shoal positions. At New River Inlet, we use main channel current velocities between 0.25 and 0.6 m/s as our threshold. (3) Tidal averages of the radar derived shoal positions result in an average accuracy of 4.3 m, with significantly higher accuracies observed for specific shoals (e.g., S3 and S4). We use these findings to estimate shoal migration at the New River Inlet.

The location of the S1 (upper) shoal within the SW ETD has limited exposure to the predominantly southeasterly incident wavefield resulting in consistent low errors during most observed sea state conditions (Tables 1 and 2). This allowed for estimates of daily migration of the shoal using the DPIV algorithm from 4 May 2012 to

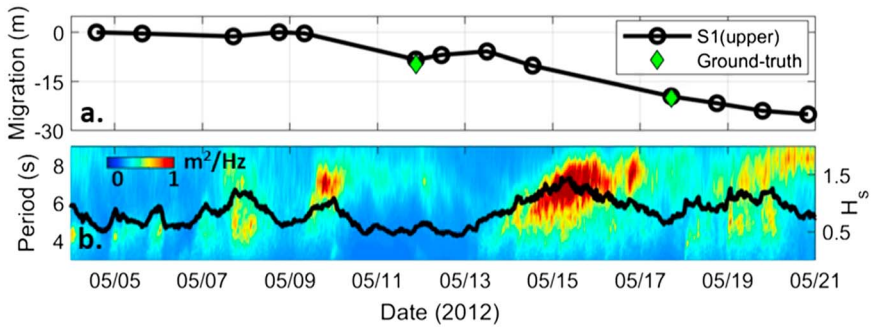

Figure 9. (a) Estimated shoal migration measured for shoal S1 (upper) from 4 May 2012 to 20 May 2012. The green diamonds provide ground-truth shoal positions (i.e., bathymetry data) on 10 May 2012 and 17 May 2012. (b) Observed wave spectrogram as a function of period from the CDIP buoy overlaid with H_s.

20 May 2012 by using radar shoal signatures at S1 (upper) near maximum ebb (i.e., greater than 0.9 m/s). We excluded 2–3 May 2012 from the analysis due to the different shoal signature response from the increased video gain settings during this period. Additionally, position estimates were excluded during times of high wave energy (e.g., 9 May 2012 and 15–17 May 2012) when signatures would quickly saturate. A consistent onshore migration was observed with a total movement during the period of 27 m (Figures 9a and 9b). The position estimates correspond well with ground-truth bathymetry data on 10 May 2012 and 17 May 2012. The largest periods of migration are observed to coincide with significant wave events, suggesting that wave energy over the SW ETD is the primary mechanism migrating the shoals.

For the remaining shoals that were more impacted by the incident wavefield, migration was estimated from the DPIV algorithm using the following criteria:

1. S1 (lower): Shoal migration was estimated from 10 May 2012 to 17 May 2012 using the averaged nonsaturated shoal signature location above a current threshold of 0.9 m/s on 10 May 2012 and 17 May 2012. Estimates were not made from 2 May 2012 because this lower portion of the S1 shoal had not fully formed (Figure 2).
2. S2 and S5: Shoal migration was estimated from 2 May 2012 to 17 May 2012 using the flood shoal signature location on 2 May 2012 (found to well represent shoal position under initially high WAMOS video gain settings) and the averaged signature location between a current threshold of 0.25 and 0.6 m/s on 17 May 2012.
3. S3 and S4: Shoal migration was estimated from 2 May 2012 to 17 May 2012 using the tidally (ebb) averaged locations on 2 May 2012 on 17 May 2012.
4. S6: Shoal migration for the deeper shoal was estimated from 2 May 2012 to 17 May 2012 using the shoal signature location near maximum ebb tide as suggested by Figure 8d.

The estimated migration for each shoal using the above criteria is illustrated in Figure 10a. The starting position on 2 May 2012 for each shoal was designated with a plus sign within a circle, while the 10 May 2012 and 17 May 2012 were defined by a star and cross sign within a circle, respectively. The errors between bathymetry and radar-derived shoal positions are provided in Table 3.

In addition to individual shoal migration estimates, bulk migration was also estimated for three regions from 2 May 2012 (red dashed box) to 17 May 2012 (black dashed box; Figure 10b). One analysis region bounded shoals S1 and S2 within the SW portion of the ETD, while the remaining two regions bounded the majority of the lengths of shoals S4 and S6.

The least amount of shoal migration was observed for S3 with a total estimated migration of +4 m, while the largest migrations were computed within the SW ETD for shoals S1 and S2 with estimated migrations of −27 and −35 m, respectively. Bathymetry observations showed a lengthening of the 1.6 m contour of S1 allowing for separate tracking of the southern portion of the shoal from 10 May to 17 May 2012; however, a large error was initially observed on 10 May 2012 but significantly reduced by the 17 May 2012 (Table 3). The remaining shoals also observed an onshore migration with estimates of −23 and −19 m, respectively, for shoals S4 and S5. A larger error was observed for S5 on 17 May 2012 due to radar shoal signature pattern shift resulting from significant bathymetry changes to the shoal.

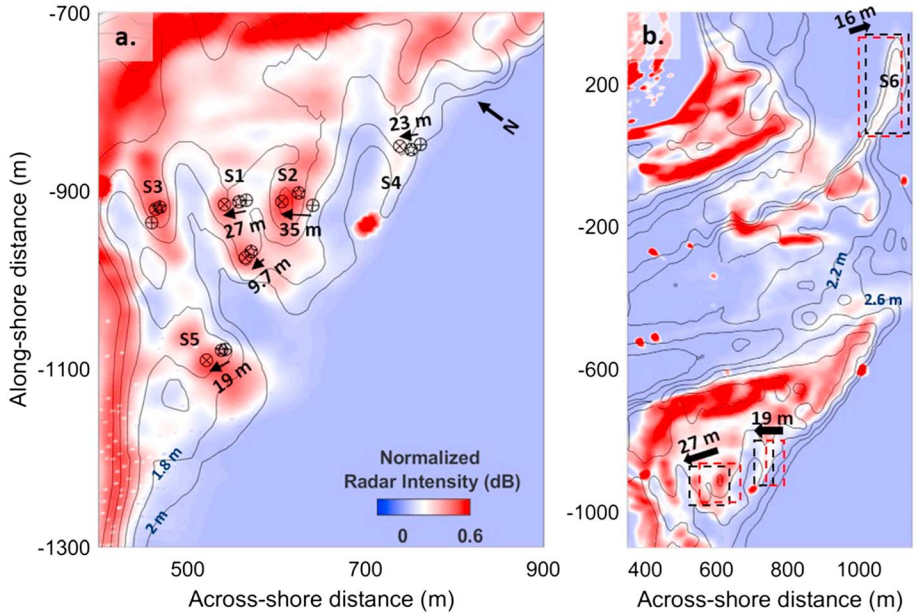

Figure 10. Ensemble-averaged radar intensities on 17 May 2012 at 1300 UTC overlaid with results from the digital-particle image velocimetry algorithm for (a) five shoals within the SW ebb tidal deltas (S1, S2, S3, S4, and S5) and (b) one deeper shoal adjacent to a remnant channel (S6). Positions of the shoals on 2 May 2012, 10 May 2012, and 17 May 2012 are denoted by a plus sign within a circle, a star within a circle, and a cross sign within a circle respectively. Figures are overlaid with bathymetry contours.

The bulk migration patterns correspond with the patterns observed for the individual shoals, confirming the onshore movement of the SW portion of the ETD. Conversely, an along-channel offshore migration of 16 m for S6 was observed from 2 May 2012 to 17 May 2012. However, the majority of the migration occurred from 2 May 2012 to 10 May 2012, with minimal additional movement observed after the 10 May 2012.

5. Discussion

Sea surface roughness, caused by the interaction of tidal current velocity with the incident wavefield over the shallow inlet bathymetry, was the dominant mechanisms causing elevated radar intensities within the New River ETD. Temporal averaging of the radar intensities delineated areas of persistent elevated intensities that were used to infer the location of the underlying shoal positions. A challenge of using X-band radar to assess morphological variability is determination of the appropriate time when the peak radar signature best correlates to shoal position, which becomes increasingly difficult in a tidal environment. Despite the complex wave, current, and bathymetry interactions, we were able to find optimal time periods when radar shoal signatures best corresponded to true shoal position. Tidal averages of radar shoal signature positions resulted in mean spatial errors of 4.3 m. However, the absence of wave interactions over the ETD (i.e., low sea states and protected shoal) resulted in the lowest observed spatial errors during the study when shoal signatures near maximum ebb tide were compared to true shoal positions. For shoals exposed to higher wave energy, shoal signatures nearer slack tide best corresponded with true shoal positions.

Table 3
Radar Shoal Position x Direction Errors Computed for the Migration Estimates Illustrated in Figure 10

	2 May 12	10 May 12	17 May 12
Shoal	*x*-error (m)	*x*-error (m)	*x*-error (m)
S1 (upper)	0	1	−4.5
S1 (lower)	n/a	−11.4	−2
S2	−1	−5	−4.2
S3	−2	−2	−1
S4	0	−1	−1
S5	−1	−5	11

5.1. Shoal Signature Response to Wave Direction

Up to this point, we have not discussed the impact that wave direction has on radar shoal signatures. The peak wave directions for the RIVET-I study were predominantly out of the southeast, resulting in waves that refracted ~10° before interacting with the SW ETD at oblique angles (Wargula et al., 2014). However, wave direction on 4 May 2012 was from the southwest, resulting in an approximately shoal normal direction to the SW ETD. The variability of radar responses under similar current and wave conditions

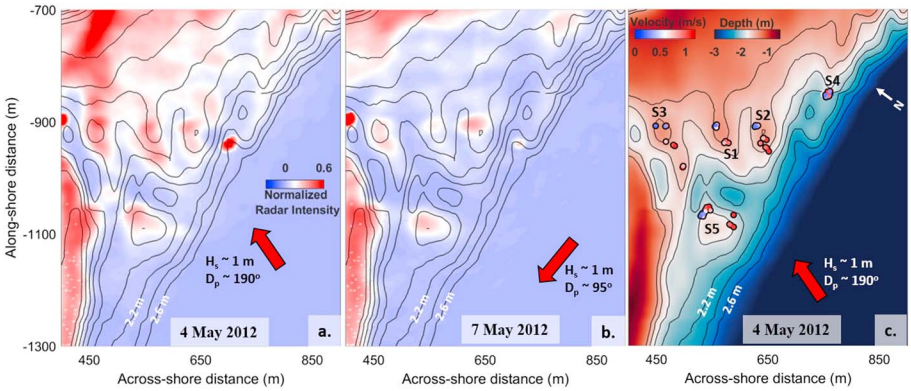

Figure 11. Scatter plots of ensemble-averaged radar errors as a function of main channel current velocity, color coded by radar intensity for shoals (a and c) S1 (upper), (b and d) S3, and (e and f) and S4. Comparison periods include (a, b, and e) 9–10 May 2012 and (c, d, and f) 16–17 May 2012.

across the SW ETD for the normal wave approach (4 May 2012) and an oblique wave approach (7 May 2012) is illustrated in Figures 11a and 11b, respectively. The more direct approach of the waves on the 4 May 2012 resulted in significantly higher radar intensity levels across the SW ETD. To assess changes in the observed ebb tidal error pattern from the typically southeasterly waves (Figure 7) to a southwest wave approach, we assume minimal changes in bathymetry from 2 May 2012 to 4 May 2012. This allows us to illustrate the new error pattern with respect to bathymetry observations (Figure 11c). The observed shoal signature variability changes from a primarily *x* direction (across-shoal) error pattern observed on 10 May 2012 and the 17 May 2012 (Figures 7a and 7b) to a more along-shoal (y direction) variability for shoals S1, S2 and S3 on 4 May 2012 as current velocity increases. The *x* position of shoals S1 and S2 corresponds well during all ebb current velocities, with higher accuracies occurring near maximum ebb tide. Similar results are observed for shoal S3, but the along-shoal location varies with ebb current magnitude. However, minimal movement was observed for a southwest wave approach, instead migration estimates (Figure 9) showed that landward migration occurred primarily when waves were from the southeast, consistent with numerical modeling results (Chen et al., 2015).

5.2. Shoal Signature Response to Wave Energy

The results of this analysis show a complex relationship between the surface signature of the shoal to bathymetry, current, and wave interactions. In the absence of waves, minimal errors consistently occurred near maximum ebb tide (Figure 8; 10 May 2012). However, under more substantial sea states, larger spatial variability of the shoal signatures was observed. To further illustrate the impact of variable wave conditions on shoal signatures, we compare error patterns on subsequent days with differing wave conditions, assuming minimal shoal migration. Offshore significant wave height during the second ebb tide on 9 May 2012 was near 1 m, which decreased significantly to 0.5 m 24 hr later. Similarly, a 1-m significant wave height on 16 May 2012 dropped to 0.7 m on 17 May 2012. Scatter plots of error to current velocity during these periods show minimal impact to errors observed at S1 due to the inshore location of the shoal, sheltering it from wave effects (Figures 12a and 12c). The location of S2, adjacent to the SW ETD ocean boundary, makes it more susceptible to spatial errors in the shoal signature due to its exposure to wave interactions. Errors tend to increase faster during higher sea state conditions as illustrated at S2 in Figures 12b and 12d. However, the migration estimates at S1 (Figure 9a) show that shoal movement was likely during these time periods, which may also contribute to the observed differences. The deeper S4 shoal was less effected by variability in wave conditions except near maximum ebb currents (Figures 12e and 12f).

5.3. DPIV Algorithm Application

Error results confirm that position estimates should be made under similar bathymetry, sea state, and velocity conditions. Significant bathymetry changes were observed for shoal S5 from 2 May 2012 to 17 May 2012. The S5 shoal, initially detached from the shoreline, steadily attached itself throughout the experiment resulting in a much wider shoal (Figure 2). Due to the increased shoal width, the peak in across-shoal radar shoal signature response changes, resulting in larger positional errors making the across-shoal peak intensity method

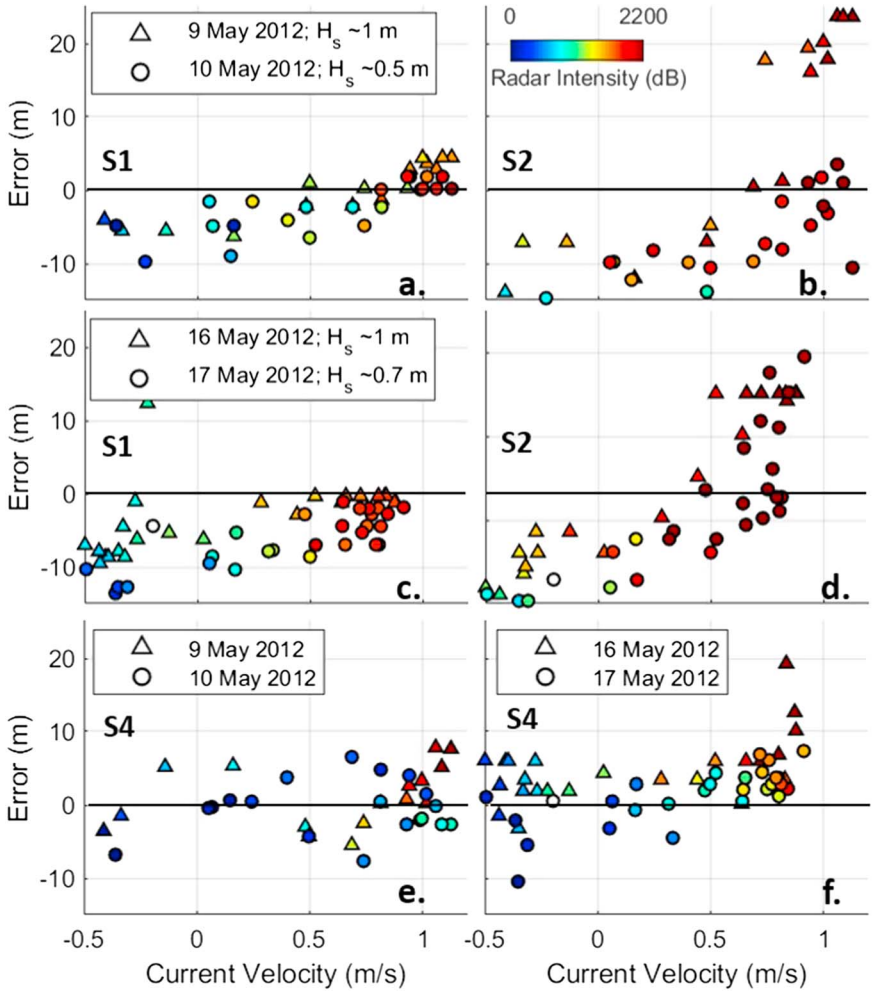

Figure 12. Comparison of radar shoal intensities across the southwestern ebb tidal delta for (a) southerly and (b) easterly peak wave directions on 4 May 2012 and 7 May 2012 respectively. (c) Bathymetry map overlaid with derived radar shoal positions (circles) during ebb tide on 4 May 2012 for southerly wave conditions. Locations are color coded by averaged observed current velocity in the main channel of the inlet. Approximate significant wave height (H_s) and peak wave direction (D_p) are given in each figure. Peak wave direction is illustrated by the red arrows in each figure.

invalid. Long-term X-band observations of the radar response to across-shoal spatial variability will quantify this relationship. In this study, the most consistent error results were observed for shoals S1 (upper), S2, S4, and S6 whose bathymetric footprint remained relatively consistent throughout the experiment.

Further evidence of the need to estimate migration under similar environmental conditions was observed for the deeper S6 shoal that was impacted by variability in wave conditions due to its location near the seaward boundary of the remnant channel. When radar position estimates were made under similar conditions (e.g., 2 May 2012 and 17 May 2012), a consistent onshore error was observed resulting in accurate relative estimates of migration. Conversely, if migration estimates were based on 2 May 2012 and 10 May 2012 observations (different sea state conditions), a spatial error of 5 m would be observed between radar-derived shoal position and the true position due to the inconsistent error pattern over the shoal.

5.4. New River Inlet Migration Mechanisms

The migration patterns of the New River Inlet observed by the X-band radar were consistent with the modeling results of Chen et al. (2015). Their numerical experiments suggested that tidal currents drive sediment fluxes in the channel, but that sediment fluxes over the SW ETD are driven primarily by wave-bathymetry interactions. In addition, for waves from the southeast, offshore significant wave height needed to be

greater than ~1 m to induce significant landward sediment transport within the SW ETD. During the RIVET-I experiment, the largest wave event occurred from 14 May 2012 to 16 May 2012 and was followed by a period of enhanced wave energy until approximately 20 May 2012. The largest observed migration of the shoals was observed during this period (Figure 9), confirming that increased wave energy over the ETD was the primary mechanism driving the landward migration of shoals within the SW portion of the ETD during the RIVET experiment. The observed rates in the SW portion of the New River ETD were similar to those found by Pianca et al. (2014) from 29 April 2012 to 22 May 2012 with typical rates between 2 and 3 m/day and a maximum average rate of 3.5 m/day in some places.

Opposite the observed migration within the SW ETD, significant offshore (along channel) migration for the S6 shoal was observed during the spring tidal cycle, while minimal movement was observed for neap tidal cycle. These observations support the numerical modeling findings that sediment fluxes are in an offshore direction in the inlet channels. In addition, Chen et al. (2015) found that for neap conditions, fluxes in the channel are at least 1 order of magnitude smaller than those during spring conditions. This suggests that the decrease in tidal magnitude from spring to neap during the RIVET experiment may have been the mechanism that stalled the offshore migration of S6 on approximately 12 May 2012.

5.5. Future Applications

The X-band morphological analysis at the New River Inlet showed the feasibility of utilizing remote sensing observations to quantify shoal migration patterns in a complex ETD system. We acknowledge the need for long-term X-band ETD observational studies containing numerous wave events and directions to allow for a separation of anomalous migration patterns from consistent patterns that correlate with wave statistics. In addition, a robust assessment of X-band shoal signature response to the variability in shoal shape will develop more accurate position estimates for shoals that exhibit significant variability in bathymetric structure. The long-term observations would also allow for a feasibility analysis of shoal morphology forecasting based on high-frequency events (e.g., spring/neap tides and storms) and seasonal trends that can be utilized in operational forecast models. Yet the results of the New River analysis verify that X-band radar-derived shoal positions can be used as a proxy for true shoal positions with typical mean absolute errors less than 4.3 m. Temporal averaging of short observation windows (e.g., 5 min) can be used to quickly map shallow ETDs allowing for rapid morphological assessments from shore or boat-based platforms. These expeditious spatial estimates of shoal positions would benefit maritime and engineering operations for tidal inlets where large morphological responses often occur rapidly (e.g., wave-dominated inlets and seasonally opening/closing inlets). In addition, geomorphological studies requiring regular monitoring (i.e., daily, weekly, monthly, and yearly) could utilize a shore or boat-based X-band system to rapidly map inlet shoals for a given monitoring interval to study long-term migration trends or episodic events driven by large wave events (e.g., storms).

6. Conclusions

Averaging a minimal period of X-band radar ETD observations (e.g., 5 min) generates a map of surface shoal signatures whose across-shoal peak can serve as a proxy for underlying shoal positions. Here we assessed the differences between New River Inlet shoal positions, defined as the minimum depth of the across shoal length, to their corresponding radar surface signature positions that are dependent on complex interactions between incident wave energy, tidal currents, and bathymetry. We found that radar-observed surface signatures best corresponded to true shoal positions when minimal wave energy interacted with the ETD, limiting the surface signature mechanisms to tidal currents and bathymetry. However, accurate shoal positions could be estimated from surface radar signatures under higher wave energy conditions when made during specific stages of the tidal cycle.

Despite complex wave-current-shoal interactions, small spatial errors were found when tidally averaging the radar-derived shoal positions in the SW portion of the ETD. The tidally averaged mean absolute error was 4.3 m when compared to bathymetry data from 10 May 2012 and 17 May 2012. However, our results suggest that if the radar-derived shoal positions are limited to specific stages of the tide, the error is reduced by 36% to 3 m. Specifically, when low incident wave energy interacts with the ETD, radar surface signatures near maximum ebb tide best represent the position of the underlying shoal. Conversely, when incident wave energy is present, surface signatures near slack tide exhibit lower mean absolute errors than other ebb tidal stages. We leveraged these optimal times to assess migration patterns and quantify rates within the New River Inlet.

Consistent with previous studies, daily assessments of X-band radar shoal signatures at optimal times during the New River study showed that the SW portion of the ETD experienced the largest morphological variability with typical shoreward migration rates of 2–3 m/day driven by incident wave energy. Conversely, an along-channel offshore movement of a deeper shoal located at the mouth of a remnant channel migrated during the spring tidal cycle at a rate of 2 m/day.

Acknowledgments
We thank the Office of Naval Research (ONR awards N00014-10-0548 and N00014-13-1-0181, managed by Thomas Drake and Reginald Beach) for their sponsorship of this work. Steve Elgar and Britt Raubenheimer from Woods Hole Oceanographic Institute are acknowledged for providing tidal observations used in this study. Lastly, we would like to thank the four anonymous reviewers, and the Editors for their constructive comments, which greatly helped to improve the quality of the manuscript. Ensemble X-band radar data used for this study are provided from the Figshare online repository: https://doi.org/10.6084/m9.figshare.7250153.

References

Allard, R., Dykes, J., Hsu, Y. L., Kaihatu, J., & Conley, D. (2008). A real-time nearshore wave and current prediction system. *Journal of Marine Systems*, *69*(1-2), 37–58. https://doi.org/10.1016/j.jmarsys.2007.02.020

Alpers, W., & Hennings, I. (1984). A theory of the imaging mechanism of underwater bottom topography by real and synthetic aperture radar. *Journal of Geophysical Research*, *89*(C6), 10,529–10,546. https://doi.org/10.1029/JC089iC06p10529

Austin, M. J., Scott, T. M., Russell, P. E., & Masselink, G. (2012). Rip current prediction: Development, validation, and evaluation of an operational tool. *Journal of Coastal Research*, *29*, 283–300.

Bass, F. G., Fuks, I. M., Kalmykov, A. I., Ostrovsky, I. E., & Rosenberg, A. D. (1968). Very high frequency radio scattering by a disturbed sea surface: 2. Scattering from an actual sea surface. *IEEE Transactions on Antennas and Propagation*, *AP-16*(5), 560–568.

Beardsley, R. C., Boicourt, W. C., & Hansen, D. V. (1976). Physical oceanography of the Middle Atlantic Bight. In G. Gross (Ed.), *The Middle Atlantic Continental Shelf and New York Bight, Spec. Symp. Ser.* (Vol. 2, pp. 20–34). New York: American Society of Limnology and Oceanography.

Bell, P. (1999). Shallow water bathymetry derived from an analysis of x-band marine radar images of waves. *Coastal Engineering*, *37*(3-4), 513–527. https://doi.org/10.1016/S0378-3839(99)00041-1

Bell, P., Williams, J. J., Clark, S., Morris, B. D., & Vila Concejo, A. (2006). Nested radar systems for remote coastal observations. *Journal of Coastal Research*, *39*, 483–487.

Bell, P. S., Bird, C. O., & Plater, A. J. (2016). A temporal waterline approach to mapping intertidal areas using X-band marine radar. *Coastal Engineering*, *107*, 84–101. https://doi.org/10.1016/j.coastaleng.2015.09.009

Bergsma, E. W. J., Conley, D. C., Davidson, M. A., & O'Hare, T. (2016). Video-based nearshore bathymetry estimation in macro-tidal environments. *Marine Geology*, *374*, 31–41. https://doi.org/10.1016/j.margeo.2016.02.001

Bertin, X., Fortunato, A. B., & Oliveira, A. (2009). A modeling-based analysis of processes driving wave-dominated inlets. *Continental Shelf Research*, *29*(5-6), 819–834. https://doi.org/10.1016/j.csr.2008.12.019

Blenkinsopp, C. E., Turner, I. L., Allis, M. J., Peirson, W. L., & Garden, L. E. (2012). Application of LIDAR technology for measurement of time-varying free-surface profiles in a laboratory wave flume. *Coastal Engineering*, *68*, 1–5.

Bruun, P. (1978). Stability of tidal inlets. In *Theory and engineering* (Vol. 510, 506 pp.). Amsterdam, Netherlands: Elsevier.

Bruun, P., & Gerritsen, F. (1960). Natural bypassing of sand at coastal inlets. *Journal of the Waterways and Harbors Division*, *85*, 75–107.

Buchhave, P. (1992). Particle image velocimetry—Status and trends. *Experimental Thermal and Fluid Science*, *5*(5), 586–604. https://doi.org/10.1016/0894-1777(92)90016-X

Catalán, P. A., Haller, M. C., Holman, R. A., & Plant, W. J. (2011). Optical and wave detection of wave breaking in the surf zone. *IEEE Transactions on Geoscience and Remote Sensing*, *49*(6), 1879–1893. https://doi.org/10.1109/TGRS.2010.2095864

Cayocca, F. (2001). Long-term morphological modelling of a tidal inlet: The Arcachon Basin, France. *Coastal Engineering*, *42*(2), 115–142. https://doi.org/10.1016/S0378-3839(00)00053-3

Chen, J.-L., Hsu, T.-J., Shi, F., Raubenheimer, B., & Elgar, S. (2015). Hydrodynamic and sediment transport modeling of New River Inlet (NC) under the interaction of tides and waves. *Journal of Geophysical Research: Oceans*, *120*, 4028–4047. https://doi.org/10.1002/2014JC010425

Chickadel, C. C., Horner-Devine, A. R., Talke, S. A., & Jessup, A. T. (2009). Vertical boil propagation from a submerged estuarine sill. *Geophysical Research Letters*, *36*, L10601. https://doi.org/10.1029/2009GL037278

Cooper, J. A. G. (1994). Sedimentation in the river-dominated Mvoti estuary, South Africa. *Geomorphology*, *9*(4), 271–300. https://doi.org/10.1016/0169-555X(94)90050-7

Dankert, H., Horstmann, J., & Rosenthal, W. (2005). Wind and wave field measurements using marine x-band radar image sequences. *IEEE Journal of Oceanic Engineering*, *30*(3), 534–542. https://doi.org/10.1109/JOE.2005.857524

Dodet, G., Bertin, X., Bruneau, N., Fortunato, A. B., Nahon, A., & Roland, A. (2013). Wave-current interactions in a wave-dominated tidal inlet. *Journal of Geophysical Research: Oceans*, *118*, 1587–1605. https://doi.org/10.1002/jgrc.20146

Donato, T. F., Askari, F., Marmorino, G. O., Trump, C. L., & Lyzenga, D. R. (1997). Radar imaging of sand waves on the continental shelf east of Cape Hatteras, NC, USA. *Continental Shelf Research*, *17*(9), 989–1004. https://doi.org/10.1016/S0278-4343(97)00001-0

Duffy, G. P., & Hughes-Clarke, J. E. (2005). Application of spatial cross correlation to detection of migration of submarine sand dunes. *Journal of Geophysical Research*, *110*, 1–11. https://doi.org/10.1029/2004JF000192

Dugan, J. P., Piotrowski, C. C., & Williams, J. Z. (2001). Water depth and surface current retrievals from airborne optical measurements of surface gravity wave dispersion. *Journal of Geophysical Research*, *106*(C8), 16,903–16,915. https://doi.org/10.1029/2000JC000369

Elias, E., & Spek, A. (2006). Long-term morphodynamic evolution of tidal inlet and its ebb-tidal delta (The Netherlands). *Marine Geology*, *225*(1-4), 5–21. https://doi.org/10.1016/j.margeo.2005.09.008

Feddersen, F., Olabarrieta, M., Guza, R. T., Winters, D., Raubenheimer, B., & Elgar, S. (2016). Observations and modeling of a tidal inlet dye tracer plume. *Journal of Geophysical Research: Oceans*, *121*, 7819–7844. https://doi.org/10.1002/2016JC011922

FitzGerald, D. M. (1988). Shoreline erosional-depositional processes associated with tidal inlets. In D. G. Aubrey & L. Weishar (Eds.), *Lecture notes on coastal and estuarine studies* (Vol. 29, pp. 186–224). New York: Springer-Verlag. https://doi.org/10.1029/LN029p0186

Gao, S., & Collins, M. (1994). Tidal inlet stability in response to hydrodynamic and sediment dynamic conditions. *Coastal Engineering*, *23*(1-2), 61–80. https://doi.org/10.1016/0378-3839(94)90015-9

Goodwin, P. (1996). Predicting the stability of tidal inlets for wetland and estuary management. *Journal of Coastal Research: Special Issue*, *23*, 83–102.

Haller, M. C., Honegger, D., & Catalán, P. A. (2013). Rip current observations via marine radar. *Journal of Waterway Port, Coastal, and Ocean Engineering*, *140*(2), 115–124. https://doi.org/10.1061/(ASCE)WW.1943-5460.0000229

Hayes, M. O. (1991). Geomorphology and sedimentation patterns of tidal inlets. In *Proc. Coastal Sediments* (pp. 1343–1355). Seattle: ASCE.

Hoan, L. X., Hanson, H., Larson, M., & Kato, S. (2011). A mathematical model of spit growth and barrier elongation: Application to Fire Island Inlet (USA) and Badreveln Spit (Sweden). *Estuarine, Coastal and Shelf Science*, *93*(4), 468–477. https://doi.org/10.1016/j.ecss.2011.05.033

Holland, K. (1998). Beach cusp formation and spacings at Duck, USA. *Continental Shelf Research*, *18*(10), 1081–1098. https://doi.org/10.1016/S0278-4343(98)00024-7

Holland, K. T., Holman, R. A., Lippmann, T. C., Stanley, J., & Plant, N. (1997). Practical use of video imagery in nearshore oceanographic field studies. *IEEE Journal of Oceanic Engineering*, *22*(1), 81–92. https://doi.org/10.1109/48.557542

Holman, R., Plant, N., & Holland, T. (2013). cBathy: A robust algorithm for estimating nearshore bathymetry. *Journal of Geophysical Research: Oceans*, *118*, 2595–2609. https://doi.org/10.1002/jgrc.20199

Holman, R., & Stanley, J. (2013). cBathy bathymetry estimation in the mixed wave-current domain of a tidal estuary. *Journal of Coastal Research: Special Issue*, *165*, 1391–1396. https://doi.org/10.2112/SI65-235.1

Holman, R. A., & Haller, M. C. (2013). Remote sensing of the nearshore. *Annual Review of Marine Science*, *5*(1), 95–113. https://doi.org/10.1146/annurev-marine-121211-172408

Holman, R. A., Sallenger, A. H., Lippmann, T. C., & Haines, J. W. (1993). The application of video image processing to the study of nearshore processes. *Oceanography*, *6*(3), 78–85. https://doi.org/10.5670/oceanog.1993.02

Holman, R. A., & Stanley, J. (2007). The history and technical capabilities of Argus. *Coastal Engineering*, *54*(6-7), 477–491. https://doi.org/10.1016/j.coastaleng.2007.01.003

Huang, H., Dabiri, D., & Gharib, M. (1997). On errors of digital particle image velocimetry. *Measurement Science and Technology*, *8*(12), 1427–1440. https://doi.org/10.1088/0957-0233/8/12/007

Keane, R. D., & Adrian, R. J. (1990). Optimization of particle image velocimeters. I. Double pulsed systems. *Measurement Science and Technology*, *1*(11), 1202–1215. https://doi.org/10.1088/0957-0233/1/11/013

Keulegan, G. H. (1951). Water-level fluctuations of basins in communication with seas, *Third Progress Report on Tidal Flow in Entrances*, beach Erosion board, Corps of Engineers, Department of the Army, U.S. Department of Commerce, National Bureau of Standards Report 1146A.

Lippmann, T. C., & Holman, R. A. (1989). Quantification of sand bar morphology: A video technique based on wave dissipation. *Journal of Geophysical Research*, *94*(C1), 995–1011. https://doi.org/10.1029/JC094iC01p00995

Lippmann, T. C., & Holman, R. A. (1990). The spatial and temporal variability of sand bar morphology. *Journal of Geophysical Research*, *95*(C7), 11,575–11,590. https://doi.org/10.1029/JC095iC07p11575

Lippmann, T. C., Holman, R. A., & Hathaway, K. K. (1993). Episodic, nonstationary behavior of a double bar system at Duck, North Carolina, U.S.A.,1986–1991. *Journal of Coastal Research*, *15*, 49–75.

MacMahan, J., van de Kreeke, J., Reniers, A., Elgar, S., Raubenheimer, B., Thornton, E., Weltmer, M., et al. (2014). Fortnightly tides and subtidal motions in a choked inlet. *Estuarine, Coastal and Shelf Science*, *150*(Part B), 5–331.

McNinch, J. E. (2007). Bar and Swash Imaging Radar (BASIR): A mobile X-band radar designed for mapping nearshore sand bars and swash-defined shorelines over large distances. *Journal of Coastal Research*, *231*(1), 59–74. https://doi.org/10.2112/05-0452.1

McNinch, J. E., Brodie, K. L., & Slocum, R. K. (2012). Radar Inlet Observing System (RIOS): Continuous remote sensing of waves, currents, and bathymetry at tidal inlets. *Oceans, 1–8*, 14–19. https://doi.org/10.1109/OCEANS.2012.6404957

Melville, W. K., Veron, F., & White, C. J. (2002). The velocity field under breaking waves: Coherent structure and turbulence. *Journal of Fluid Mechanics*, *454*, 203–233. https://doi.org/10.1017/S0022112001007078

Nahon, A., Bertin, X., Fortunato, A. B., & Oliveira, A. (2012). Process-based 2DH morphodynamic modeling of tidal inlets: A comparison with empirical classifications and theories. *Marine Geology*, *291-294*, 1–11. https://doi.org/10.1016/j.margeo.2011.10.001

Nienhuis, J. H., & Ashton, A. D. (2016). Mechanics and rates of tidal inlet migration: Modeling and application to natural examples. *Journal of Geophysical Research: Earth Surface*, *121*, 2118–2139. https://doi.org/10.1002/2016JF004035

O'Brien, M. P. (1931). Estuary tidal prisms related to entrance areas. *Civil Engineering*, *1*(8), 738–739.

O'Brien, M. P. (1969). Equilibrium flow areas of inlets in sandy coasts. *Journal of the Waterways, Harbors, and Coastal Engineering Division, American Society of Civil Engineers*, *95*, 43–52.

Oliveira, A., Fortunato, A. B., & Rego, J. R. L. (2006). Effect of morphological changes on the hydrodynamics and flushing properties of the O´bidos lagoon (Portugal). *Continental Shelf Research*, *26*(8), 917–942. https://doi.org/10.1016/j.csr.2006.02.011

Pearre, N., & Puleo, J. (2009). Quantifying seasonal shoreline variability at Rehoboth Beach, Delaware, using automated imaging techniques. *Journal of Coastal Research*, *25*, 900–914.

Pianca, C., Holman, R., & Siegle, E. (2014). Mobility of meso-scale morphology on a microtidal ebb delta measured using remote sensing. *Marine Geology*, *357*, 334–343. https://doi.org/10.1016/j.margeo.2014.09.045

Pietrafesa, L. J., Janowitz, G. S., & Wittman, P. A. (1985). Physical oceanographic processes in the Carolina Capes. In L. P. Atkinson, D. W. Menzel, & K. A. Bush (Eds.), *Oceanography of the southeastern US continental shelf* (pp. 23–32). Washington, DC: American Geophysical Union. https://doi.org/10.1029/CO002p0023

Plant, N. G., Aarninkhof, S. G. J., Turner, I. L., & Kingston, K. S. (2007). The performance of shoreline detection models applied to video imagery. *Journal of Coastal Research*, *23*.

Puleo, J. A., Farquharson, G., Frasier, S. J., & Holland, K. T. (2003). Comparison of optical and radar measurements of surf and swash zone velocity fields. *Journal of Geophysical Research*, *108*(C3), 3100. https://doi.org/10.1029/2002JC001483

Ranasinghe, R., & Pattiaratchi, C. (2003). The seasonal closure of tidal inlets: Causes and effects. *Coastal Engineering Journal*, *45*(4), 601–627. https://doi.org/10.1142/S0578563403000919

Ranasinghe, R., Pattiaratchi, C., & Masselink, G. (1999). The seasonal closure of tidal inlets: Wilson inlet, a case study. *Coastal Engineering*, *37*(1), 37–56. https://doi.org/10.1016/S0378-3839(99)00007-1

Ridderinkhof, W., de Swart, H. E., van der Vegt, M., & Hoekstra, P. (2016). Modeling the growth and migration of sandy shoals on ebb-tidal deltas. *Journal of Geophysical Research: Earth Surface*, *121*, 1351–1372. https://doi.org/10.1002/2016JF003823

Rogowski, P., Terrill, E., & Chen, J. (2014). Observations of the frontal region of a buoyant river plume using an autonomous underwater vehicle. *Journal of Geophysical Research: Oceans*, *119*, 7549–7567. https://doi.org/10.1002/2014JC010392

Ruessink, B. G., Bell, P. S., Van Enckevort, I. M. J., & Aarninkhof, S. G. J. (2002). Nearshore bar crest location quantified from time-averaged X-band radar images. *Coastal Engineering*, *45*(1), 19–32. https://doi.org/10.1016/S0378-3839(01)00042-4

Siegle, E., Huntley, D., & Davidson, M. (2004). Physical controls on the dynamics of inlet sandbar systems. *Ocean Dynamics*, *54*, 360–373.

Siegle, E., Huntley, D., & Davidson, M. (2007). Coupling video imaging and numerical modelling for the study of inlet morphodynamics. *Marine Geology*, *236*(3-4), 143–163. https://doi.org/10.1016/j.margeo.2006.10.022

Spydell, M. S., Feddersen, F., Olabarrieta, M., Chen, J., Guza, R. T., Raubenheimer, B., & Elgar, S. (2015). Observed and modeled drifters at a tidal inlet. *Journal of Geophysical Research: Oceans*, *120*, 4825–4844. https://doi.org/10.1002/2014JC010541

Tung, T. T., Walstra, D. R., van de Graaff, J., & Stive, M. J. F. (2009). Morphological modeling of tidal inlet migration and closure. *Journal Coastal Research*, *IS56*, 1080–1084.

Van der Vegt, M., Schuttelaars, H., & Swart, H. (2006). Modeling the equilibrium of tide dominated ebb-tidal deltas. *Journal of Geophysical Research*, *111*, F02013. https://doi.org/10.1029/2005JF000312

Van Enckevort, I., & Ruessink, B. (2003a). Video observations of nearshore bar behaviour. Part 1: Alongshore uniform variability. *Continental Shelf Research*, *23*(5), 501–512. https://doi.org/10.1016/S0278-4343(02)00234-0

Van Enckevort, I., & Ruessink, B. (2003b). Video observations of nearshore bar behaviour. Part 2: Alongshore non-uniform variability. *Continental Shelf Research*, *23*(5), 513–532. https://doi.org/10.1016/S0278-4343(02)00235-2

Van Leeuwen, S. M., Van der Vegt, M., & Swart, H. E. (2003). Morphodynamics of ebb-tidal deltas: A model approach. *Estuarine, Coastal and Shelf Science*, *57*, 5–6, 899–907. https://doi.org/10.1016/S0272-7714(02)00420-1

Wang, Z. B., Louters, T., & de Vriend, H. J. (1995). Morphodynamic modelling for a tidal inlet in the Wadden Sea. *Marine Geology*, *126*(1-4), 289–300. https://doi.org/10.1016/0025-3227(95)00083-B

Wargula, A., Raubenheimer, B., & Elgar, S. (2014). Wave-driven along-channel subtidal flows in a well-mixed ocean inlet. *Journal of Geophysical Research: Oceans*, *119*, 2987–3001. https://doi.org/10.1002/2014JC009839

Werner, F. E., Blanton, B. O., Quinlan, J. A., & Luettich, R. A. (1999). Physical oceanography of the North Carolina continental shelf during fall and winter seasons: Implications to the transport of larval menhaden. *Fisheries Oceanography*, *8*(Suppl. 2), 7–21. https://doi.org/10.1046/j.1365-2419.1999.00016.x

Wilson, G. W., Özkan-Haller, H. T., & Holman, R. A. (2010). Data assimilation and bathymetric inversion in a 2DH surf zone model. *Journal of Geophysical Research*, *115*, C12057. https://doi.org/10.1029/2010JC006286

Wilson, G. W., Özkan-Haller, H. T., Holman, R. A., Haller, M. C., Honegger, D. A., & Chickadel, C. C. (2014). Surf zone bathymetry and circulation predictions via data assimilation of remote sensing observations. *Journal of Geophysical Research: Oceans*, *119*, 1993–2016. https://doi.org/10.1002/2013JC009213

Wright, J. W. (1968). A new model for sea clutter. *IEEE Transactions on Antennas and Propagation*, *AP-16*(2), 217–223.

Zippel, S., & Thomson, J. (2015). Wave breaking and turbulence at a tidal inlet. *Journal of Geophysical Research: Oceans*, *120*, 1016–1031. https://doi.org/10.1002/2014JC010025